Parallel Integral Projection Transform for Electrode Localization in 3D Ultrasound Images

Martin Barva, Jean-Martial Mari, Jan Kybic,
Jean-René Duhamel, Václav Hlaváč, Christian Cachard

March 1, 2007

Abstract

In surgical practice small metallic instruments are frequently used to perform various tasks inside human body. We address the problem of their accurate localization in the tissue. Recent experiments using medical ultrasound have shown that this modality is suitable for real-time visualization of anatomical structures as well as the position of surgical instruments. We propose an image processing algorithm that permits to automatically estimate the position of a line-segment shaped object. This method was applied to the localization of a thin metallic electrode in biological tissue. We show that the electrode axis can be found through maximizing the Parallel Integral Projection transform. To accelerate this step hierarchical mesh-grid algorithm is implemented. Once the axis position is known, localization of the electrode tip is performed. The method was tested on simulated images and real 3D ultrasound images of a tissue mimicking phantom containing a metallic electrode. The results indicate that the algorithm is robust toward variation in electrode position and speckle noise. Localization accuracy is of the order of hundreds of micrometers and is comparable to the ultrasound system axial resolution.

Keywords: 3D ultrasound, electrode, needle, localization, image guidance, parallel projection

1 Introduction

Many medical surgical procedures consist of introducing a small surgical instrument such as needle, or electrode into biological tissue. In biopsy, tissue samples are taken from a particular region of body by means of a thin needle [1]. In breast cancer therapy, radioactive substance is injected near the tumor [2]. In the field of neurological research, the electrical activity of a specific group of neurons is recorded by a thin electrode needle [3]. For such procedures, it is often useful to know the instrument position during the intervention.

1.1 Existing localization techniques

Horsley and Clarke, in 1908, introduced the stereotactic frame for instrument localization on small animals [4]. They used a frame fixed with respect to external anatomical landmarks to place an electrode at a specific point in the animal's brain. However, the position of intracranial point often can not be deduced from external landmarks with sufficient accuracy. To surmount this problem stereotaxy is currently combined with MRI, or CT images. This technique permits to reach the localization accuracy of the order of tenth of a millimeter [5]. To avoid the limitations and patient discomfort associated with a stereotactic frame, frameless techniques were proposed. One of them is the spatial localization using a radio-frequency signal [6]. Three fixed orthogonal coils generate electromagnetic waves that are picked-up by small coils attached to the tracked surgical instrument. Its position is estimated from the phase shift of received signals. Optical tracking with two calibrated cameras is also used [7]. The 3D position of a marker on the tracked tool is determined from its projection for both images. The main difficulty is that the marker point must be visible in both cameras. In the last few decades, tool localization using medical imaging modalities such as MRI, CT and ultrasound was proposed. They allow the physicians to view anatomical information of human body as well as surgical instruments during the intervention. In terms of applicability to the problem of metallic instrument localization, the ultrasound imaging modality offers a number of advantages: short acquisition time permits real-time imaging; no ionizing radiation is involved; compatibility with metallic objects. The resolution of modern systems is

approximately one millimeter. The purchase and operational cost is low compared to other medical imaging modalities.

1.2 Problem description

The usage of ultrasound for image-guidance procedures is currently in the research stage. Glimcher [8] investigated the observability of a thin electrode inside a primate cortex in 2D ultrasound images. From the experiments he concludes that the ultrasound modality permits to visualize the anatomical structure together with a thin needle of diameter comparable to the ultrasound axial resolution. However, observing a 3D object using a conventional B-mode images presents inherent limitations. In general, only a cross section is observable, unless the electrode axis is aligned with the scan plane. This is difficult to achieve without a special mechanical setup. To overcome this problem, 3D ultrasound scanner has been used instead [9].

The task consists of automatic identification of surgical instrument in the 3D ultrasound image. The information about its position permits to extract from the acquired 3D image a planar section in which it is easier for a human to observe the tool. If the position of the ultrasound probe is known with respect to the body, we can as well determine the instrument position inside the tissue.

The task of automatic object localization in ultrasound data is difficult because of attenuation, speckle noise, shadows, low contrast between the object and background, signal dropouts causing missing object boundaries. Large amount of data requires a fast algorithm to perform a real-time localization.

1.3 Previous work

A variety of algorithms for object localization in ultrasound data have been proposed. The position of an axis of an object such as an electrode can be determined in 2D image using the Principal Component Analysis (PCA) [10]. Initially, a variance image is computed as the intensity variance in a small neighborhood of each pixel of the original image. Next, the variance image is thresholded and the PCA is applied to the covariance matrix of the

coordinates of the thresholded pixels. The electrode axis is determined by the eigenvector corresponding to the largest eigenvalue. Novotny [11] enhanced this technique to 3D images. Original image is segmented by thresholding and compact clusters of voxels are identified. The length to width ratio of each cluster is found using the PCA and the cluster with the highest ratio is selected. Tao [12] introduced ultrasound image segmentation based on model-fitting. Geometry of the 3D object to localize is described by a superquadric, whose parameters are estimated by a RANSAC estimator [13]. Another approach is based on the observation that the electrode is more conspicuous in a projected image and that its projection is minimized when the projection is performed along the electrode axis [14]. In the first step, the original image is projected to a plane. The direction of the electrode projection in the plane together with the projection direction determine a plane that contain the actual electrode. Adaptive 1D search is used to minimize the projection area of the electrode.

The article is organized as follows: Section 2 contains detailed description of proposed method. The results of tests performed on simulated and real 3D ultrasound images are summarized in Section 3. In Section 4, a discussion about the algorithm performance concludes the paper.

2 Proposed method

We introduce an algorithm that permits to automatically estimate the position of a thin electrode in a 3D ultrasound image. It identifies the electrode axis and its tip. Following assumptions about the electrode appearance in the image are made: (i) the electrode appears as a cylindrical object with a straight axis and the length much greater than the diameter, (ii) intensity of electrode voxels is much higher then the intensity of background voxels. Based on these hypothesis, the localization of electrode axis is done using the parallel projection. Unlike the method introduced by Ding in [14], we formalize the projection into the form of Parallel Integral Projection (PIP) transform and show that the electrode axis can be found by maximizing the PIP transformation of original image. The maximization is accelerated by means of the hierarchical mesh-grid algorithm. In second phase, the electrode tip is found.

This is accomplished by optimal thresholding that exploits prior probability densities of object and background voxel intensity.

2.1 Axis localization with Parallel Integral Projection transform

The Parallel Integral Projection is a transform that maps an image function $\mathcal{I} : \mathbb{R}^3 \to \mathbb{R}$ representing volume data to a function $\mathcal{P}_\mathcal{I} : \mathbb{R}^4 \to \mathbb{R}$ describing its projections as a function of the 2D displacement (u, v) and the projection direction determined by two angles (α, β) (Figure 1a). More formally, the PIP transformation of $\mathcal{I}(\mathbf{x})$ is defined by an integral along a line passing through the point $Q = [u, v]$ with direction $\mathbf{w}$ given by angles α, β:

$$\mathcal{P}_\mathcal{I}(u, v, \alpha, \beta) = \int_{-\infty}^{\infty} \mathcal{I}\left(\mathbf{R}(\alpha, \beta) \cdot (u, v, \tau)^T\right) \mathrm{d}\tau, \tag{1}$$

where

$$\mathbf{R}(\alpha, \beta) = \begin{pmatrix} \cos\beta & \sin\alpha\sin\beta & -\cos\alpha\sin\beta \\ 0 & \cos\alpha & \sin\alpha \\ \sin\beta & -\sin\alpha\cos\beta & \cos\alpha\cos\beta \end{pmatrix} \tag{2}$$

is the rotation matrix representing a rotation around the x-axis by angle α, and around the y-axis by angle β. The PIP transform is similar to the Radon transform used in Computed Tomography [15].

The PIP transform can be used to identify the axis of a thin electrode in a 3D image as follows (Figure 1b): Let $\mathcal{I} : \mathbb{R}^3 \to \mathbb{R}$ be an image function such that

$$\mathcal{I}(\mathbf{x}) = \begin{cases} 1; \forall \mathbf{x} \in \mathbf{M}, \\ 0; \forall \mathbf{x} \notin \mathbf{M}, \end{cases} \tag{3}$$

where $\mathbf{M} \subset \mathbb{R}^3$ is the electrode. In case the electrode diameter is infinitely small, the PIP transformation $\mathcal{P}_\mathcal{I}(u, v, \alpha, \beta)$ has the maximum at a point

$$(u_{max}, v_{max}, \alpha_{max}, \beta_{max}) = \arg\max \mathcal{P}_\mathcal{I}(u, v, \alpha, \beta), \tag{4}$$

when the line of integration coincides with the axis of $\mathbf{M}$ and is zero elsewhere. A parametric equation $a(t)$ of the axis is given by

$$a(t) = \mathbf{R}(\alpha_{max}, \beta_{max}) \cdot (u_{max}, v_{max}, t)^T; \qquad \forall t \in \mathbb{R}. \tag{5}$$

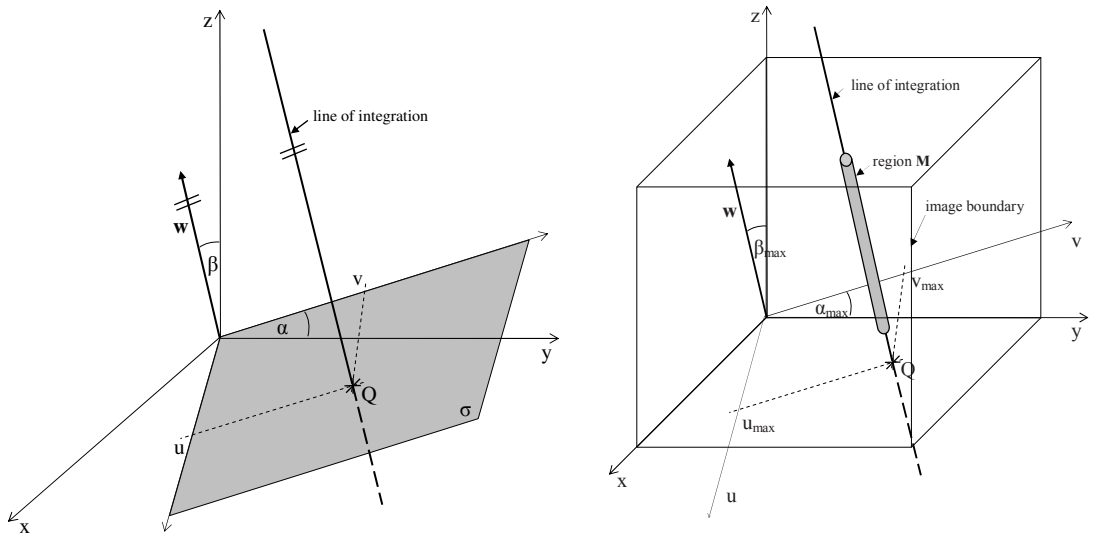

Figure 1: (a) The integral of the function $\mathcal{I}$ in (1) is calculated along a line given by the point $Q = [u, v]$ and the vector $\mathbf{w}$. (b) Evaluation of the PIP transformation of a 3D image. Electrode is represented by a cylinder M. In this particular configuration, $\mathcal{P}_{\mathcal{I}}$ is maximized since the line of integration is identical with the electrode axis.

2.1.1 Discretization of the PIP transformation

We shall maximize the PIP transformation of a 3D image on a discrete grid. The discretization steps $\Delta_\alpha, \Delta_\beta, \Delta_u, \Delta_v$ must be sufficiently fine not to miss the electrode. They are set such that

$$\Delta_\alpha,\, \Delta_\beta \;\leq\; 2 \arctan \frac{d}{2\,\|\mathbf{x}_{max}\|}, \tag{6}$$

$$\Delta_u,\, \Delta_v \;\leq\; d, \tag{7}$$

where d is the electrode diameter and $\mathbf{x}_{max}$ is the position of the most distant voxel from the origin. The motivation comes from the requirement that at least one integration line passes through the electrode (Figure 2).

The integral $\mathcal{P}_{\mathcal{I}}$ is evaluated numerically. The integration line is sampled with a sampling step corresponding to the axial resolution of ultrasound system. The integral is found using the trapezoid rule.

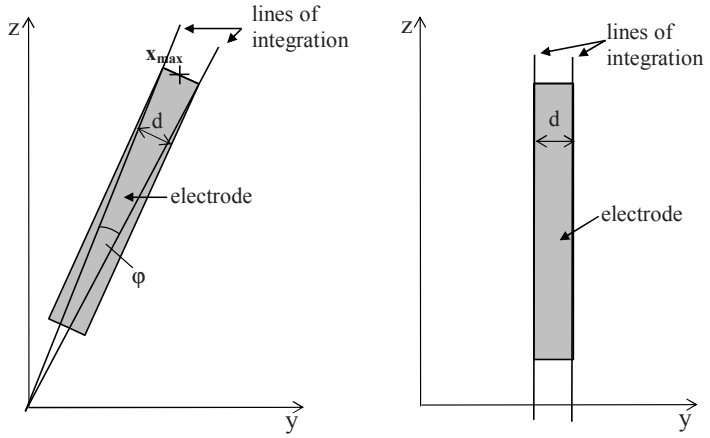

Figure 2: (a) Discretization of angles α, β. If two lines of integration incline at angle φ for which Eq. (6) holds, then at least one of the line intersects the electrode. (b) Discretization of variables u, v. Assuming two parallel lines of integration, the displacement must be less than the electrode diameter d, so that the electrode comprises at least one line of integration.

2.1.2 Maximizing the PIP transformation

Let us define a function

$$\mathcal{A}(\alpha, \beta) = \max_{u,v} \mathcal{P}_{\mathcal{I}}(u, v, \alpha, \beta), \tag{8}$$

that will be referred to as the angle function. Angles $\alpha_{max}, \beta_{max}$ maximizing $\mathcal{A}(\alpha, \beta)$ also maximize $\mathcal{P}_{\mathcal{I}}(u, v, \alpha, \beta)$ for some u_{max}, v_{max},

$$\exists u_{max}, v_{max} : (u_{max}, v_{max}, \alpha_{max}, \beta_{max}) = \arg\max \mathcal{P}_{\mathcal{I}} \Leftrightarrow (\alpha_{max}, \beta_{max}) = \arg\max \mathcal{A}. \tag{9}$$

To determine the value of $\mathcal{A}(\alpha, \beta)$, we find the circumscribed rectangle $\langle u_1, u_2\rangle \times \langle v_1, v_2\rangle$ of the parallel projection of the image boundary on the plane σ with normal vector $\mathbf{w} = \mathbb{R}(\alpha, \beta) \cdot (1, 0, 0)^T$ (Figure 3) as

$$\begin{aligned} u_1 &= \min_{\mathbf{x}\in\Omega}(\mathbf{R}^{-1}(\alpha, \beta) \cdot \mathbf{x}) \cdot \mathbf{e}_x, \quad u_2 = \max_{\mathbf{x}\in\Omega}(\mathbf{R}^{-1}(\alpha, \beta) \cdot \mathbf{x}) \cdot \mathbf{e}_x, \\ v_1 &= \min_{\mathbf{x}\in\Omega}(\mathbf{R}^{-1}(\alpha, \beta) \cdot \mathbf{x}) \cdot \mathbf{e}_y, \quad v_2 = \max_{\mathbf{x}\in\Omega}(\mathbf{R}^{-1}(\alpha, \beta) \cdot \mathbf{x}) \cdot \mathbf{e}_y, \end{aligned}$$

where Ω is a set of voxel coordinates and $\mathbf{e}_x$, $\mathbf{e}_y$ are the unit vectors in Cartesian coordinate system. The integral in Eq. (1) is evaluated at a grid of points (u, v) uniformly distributed

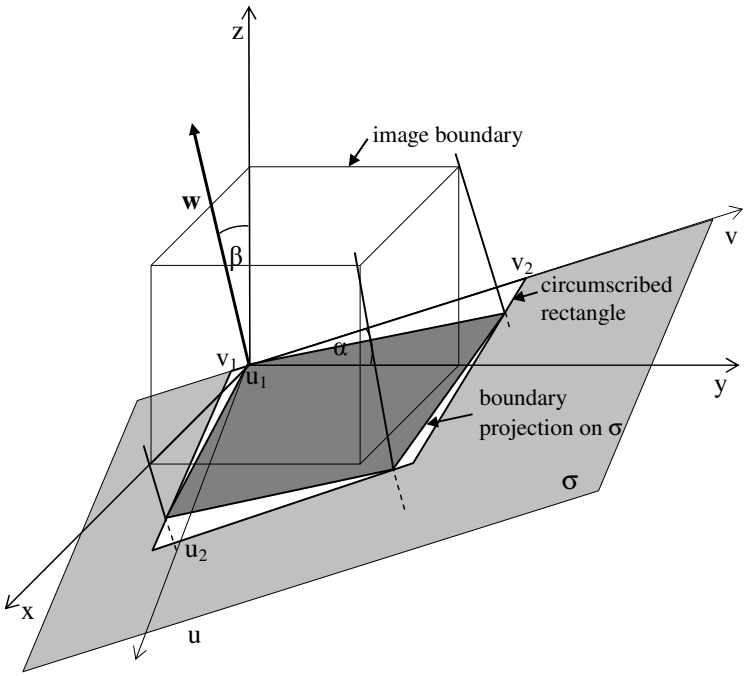

Figure 3: Evaluation of the angle function $\mathcal{A}(\alpha, \beta)$. 3D image boundary is projected on the plane σ and a circumscribed rectangle comprising the projection is determined. Sampling the rectangle with a uniform grid of points, the value of $\mathcal{A}(\alpha, \beta)$ is equal to the maximum of $\mathcal{P}_{\mathcal{I}}(\alpha, \beta, u, v)$ evaluated on this grid with fixed (α, β).

on the rectangle $\langle u_1, u_2\rangle \times \langle v_1, v_2\rangle$ with steps Δ_u, Δ_v satisfying Eq. (7). The value of $\mathcal{A}(\alpha, \beta)$ is the maximum of $\mathcal{P}_{\mathcal{I}}$ exhaustively evaluated on the grid with fixed α, β.

We shall now find values $\alpha_{max}, \beta_{max}$ that maximize the angle function $\mathcal{A}(\alpha, \beta)$,

$$(\alpha_{max}, \beta_{max}) = \arg\max \mathcal{A}(\alpha, \beta). \tag{10}$$

Two approaches to the maximization have been tested: (i) exhaustive search and (ii) hierarchical mesh-grid search.

Exhaustive search Due to the periodicity of the PIP transform in α, β, it suffices to maximize the angle function on a square grid $\langle 0, 180\rangle \times \langle 0, 180\rangle$. This grid is uniformly sampled with discretization steps satisfying Eq. (6),(7) and the angle function is evaluated in each node of the grid (Figure 6).

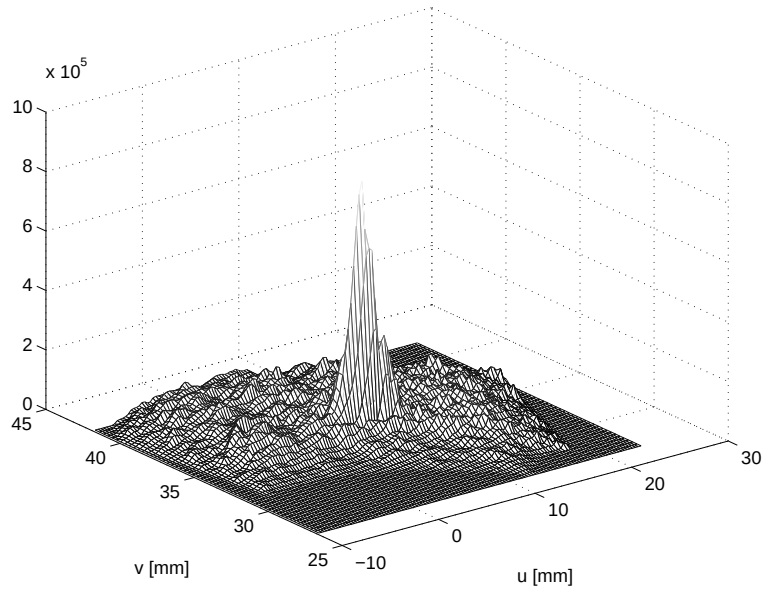

Figure 4: PIP transformation of a 3D image for a given pair of (α, β).

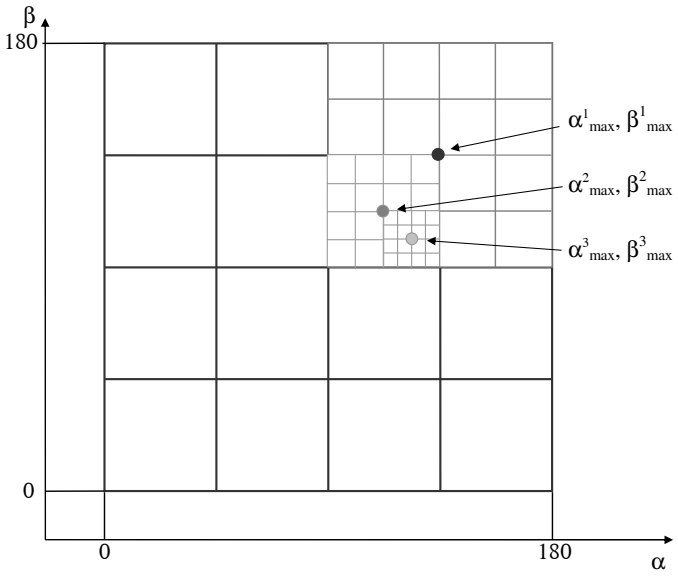

Figure 5: Principle of hierarchical mesh-grid algorithm applied to maximum search of the function $\mathcal{A}(\alpha, \beta)$.

Hierarchical mesh-grid search The main drawback of the exhaustive search is its computational complexity. To alleviate it, we propose to use the hierarchical mesh-grid search method [16]. On the first level, $\mathcal{A}(\alpha, \beta)$ is evaluated on a rectangular grid of points $\langle 0, 180\rangle \times$

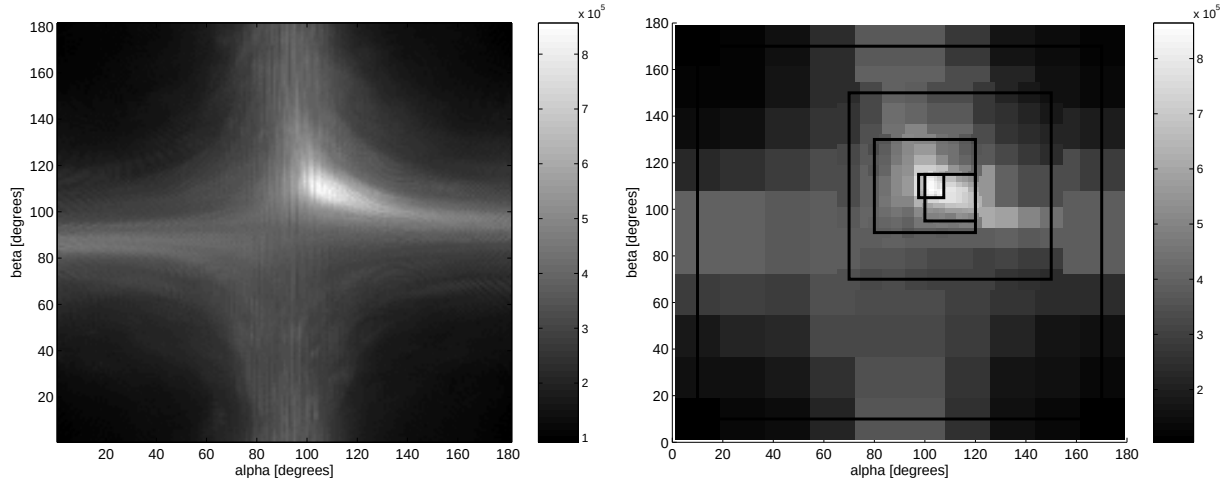

Figure 6: Maximization of the angle function $\mathcal{A}(\alpha, \beta)$. (a) Exhaustive search with discretization steps evaluates $\mathcal{A}(\alpha, \beta)$ in each node of a square gird $\langle 0, 180° \rangle \times \langle 0, 180° \rangle$ uniformly sampled with discretization steps $\Delta_\alpha = \Delta_\beta = 1°$. (b) Five-level hierarchical mesh-grid search with initial $\Delta_\alpha^1 = \Delta_\beta^1 = 16°$ and final discretization steps $\Delta_\alpha^5 = \Delta_\beta^5 = 1°$. The region of search size and discretization steps Δ_α, Δ_β are gradually decreased by factor of 2. Black rectangles in the figure delineates the region of search on each level.

$\langle 0, 180 \rangle$ that are uniformly sampled with steps[1] Δ_α^{init}, Δ_β^{init} (Figure 5). The maximum location $(\alpha_{max}^1, \beta_{max}^1)$ is determined. On the second level, the angle function is evaluated on a rectangular grid $\langle \alpha_{max}^1 - 45, \alpha_{max}^1 + 45 \rangle \times \langle \beta_{max}^1 - 45, \beta_{max}^1 + 45 \rangle$ uniformly sampled with steps $\Delta_\alpha^2 = \frac{\Delta_\alpha^1}{2}$, $\Delta_\beta^2 = \frac{\Delta_\beta^1}{2}$, where $\Delta_\alpha^1 = \Delta_\alpha^{init}$, $\Delta_\beta^1 = \Delta_\beta^{init}$. The pair $(\alpha_{max}^2, \beta_{max}^2)$ that maximizes $\mathcal{A}(\alpha, \beta)$ is established. On the i-th level, the angle function is evaluated on a grid $\langle \alpha_{max}^{i-1} - \frac{180}{2^i}, \alpha_{max}^{i-1} + \frac{180}{2^i} \rangle \times \langle \beta_{max}^{i-1} - \frac{180}{2^i}, \beta_{max}^{i-1} + \frac{180}{2^i} \rangle$ with discretization steps $\Delta_\alpha^i = \frac{\Delta_\alpha^1}{2^{i-1}}$, $\Delta_\beta^i = \frac{\Delta_\beta^1}{2^{i-1}}$. The algorithm continues until both steps Δ_α^i, Δ_β^i are equal, or inferior to some predefined threshold values Δ_α^{final}, Δ_β^{final} that control the accuracy of axis localization.

The hierarchical mesh-grid method was selected since it does not require an initial solution and can avoid to some extent a local extremum. Moreover it would be possible to use other numerical optimization methods as well as the gradient descent algorithm [17].

[1] nechavam znaceni Δ_α^{init}, Δ_β^{init} konzistentni s Δ_α^{final}, Δ_β^{final}

Comparison of exhaustive search and hierarchical search The main interest in using the hierarchical mesh-grid search method is to accelerate the task of the PIP maximization. Let us compare the computational efficiency of both search methods in terms of the number of evaluations of $\mathcal{A}(\alpha, \beta)$. This number is in fact influenced by the discretization parameters $\Delta_\alpha, \Delta_\beta$, resp. $\Delta_\alpha^{init}, \Delta_\beta^{init}, \Delta_\alpha^{final}, \Delta_\beta^{final}$ of the exhaustive, resp. hierarchical mesh-grid method.

Exhaustive search – To determine the maximum of the function $\mathcal{A}(\alpha, \beta)$ with accuracy Δ_α, Δ_β, the rectangle $\langle 0, 180\rangle \times \langle 0, 180\rangle$ is sampled along dimensions α, resp. β dimension with the step Δ_α, resp. Δ_β. The total number of the angle function evaluations is equal to

$$\frac{180}{\Delta_\alpha} \cdot \frac{180}{\Delta_\beta} \tag{11}$$

Hierarchical mesh-grid search – On each level, the discretization steps are divided by the factor of 2. Given the initial Δ_α^{init}, Δ_β^{init} and final steps Δ_α^{final}, Δ_β^{final}, the number of levels is

$$N = \max\left\{\log_2 \frac{2\Delta_\alpha^{init}}{\Delta_\alpha^{final}}, \log_2 \frac{2\Delta_\beta^{init}}{\Delta_\beta^{final}}\right\}. \tag{12}$$

There are $\left(\frac{180}{\Delta_\alpha^{init}} \cdot \frac{180}{\Delta_\beta^{init}}\right)$ evaluations on each level, so the total number of function $\mathcal{A}(\alpha, \beta)$ evaluations performed by the hierarchical mesh-grid method is

$$N \cdot \left(\frac{180}{\Delta_\alpha^{init}} \cdot \frac{180}{\Delta_\beta^{init}}\right). \tag{13}$$

In order to simplify the comparison, discretization steps of both methods are assumed to be equal: $\Delta_\alpha = \Delta_\beta = \Delta_{exh}$, $\Delta_\alpha^{init} = \Delta_\beta^{init} = \Delta^{init}$, $\Delta_\alpha^{final} = \Delta_\beta^{final} = \Delta^{final}$. Further, we let $\Delta_{exh} = \Delta^{final}$. Figure 7 shows the number of evaluations of $\mathcal{A}(\alpha, \beta)$ as a function of $\Delta_{exh}, \Delta^{final}$, where Δ^{init} is used as a parameter. We can observe that using a hierarchical mesh-grid method leads to significant decrease in computational cost.

2.2 Electrode tip localization

Once the electrode axis $a(t)$ is identified using the PIP transform, we shall determine the coordinates of electrode endpoints. In general, the electrode is not entirely comprised in the

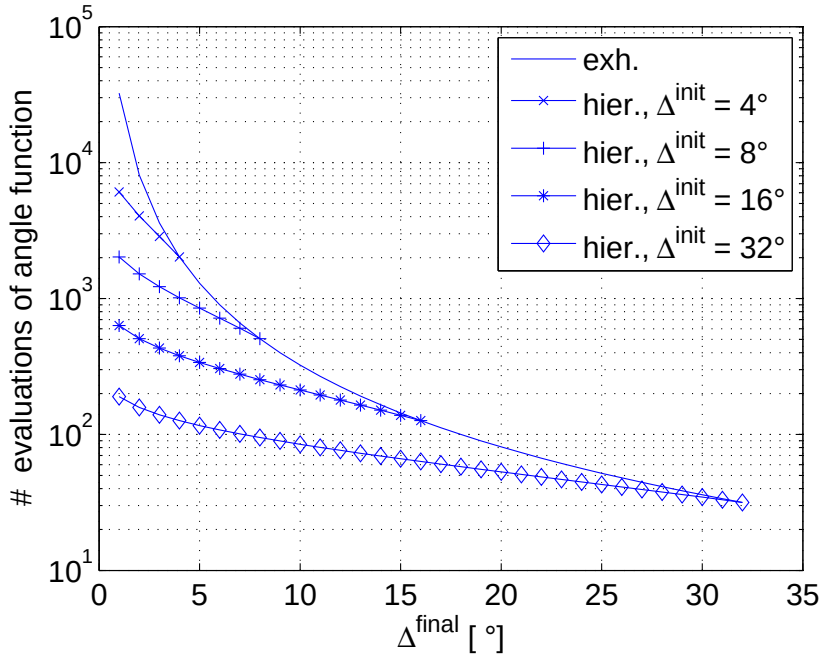

Figure 7: Comparison of the number of evaluations of $\mathcal{A}(\alpha, \beta)$ as a function of discretization steps $\Delta_{exh} = \Delta^{final}$ for exhaustive and hierarchical mesh-grid search.

field of view since only a small part of tissue is scanned by the scanning device. Therefore, we only localize the electrode endpoint (referred to as electrode tip) that is located inside the field of view.

Let $\mathcal{B}(t)$ be the voxel intensity along estimated axis $a(t)$ (Eq. (5)),

$$\mathcal{B}(t) = \mathcal{I}(a(t)); \qquad \forall t \in \mathbb{R} : \; a(t) \in \mathbf{\Omega}, \tag{14}$$

Figure 8 shows an example of intensity profile along estimated axis. While tracing the values of $\mathcal{B}(t)$ for increasing t, let t^* be the first value, where $\mathcal{B}(t)$ decreases under a pre-determined threshold T. The coordinates of the electrode tip are given by $a(t^*)$.

The threshold value T is determined from two a priori estimated probability distributions: probability of electrode voxel $P(el \,|\, I)$, resp. background voxel $P(bg \,|\, I)$ given the voxel intensity I. Parameter T is such that $P(el \,|\, T) = P(bg \,|\, T)$. To estimate these distributions, voxels with intensity I were identified in an acquired dataset with known electrode position and based on their distance from electrode axis were classified as electrode or background

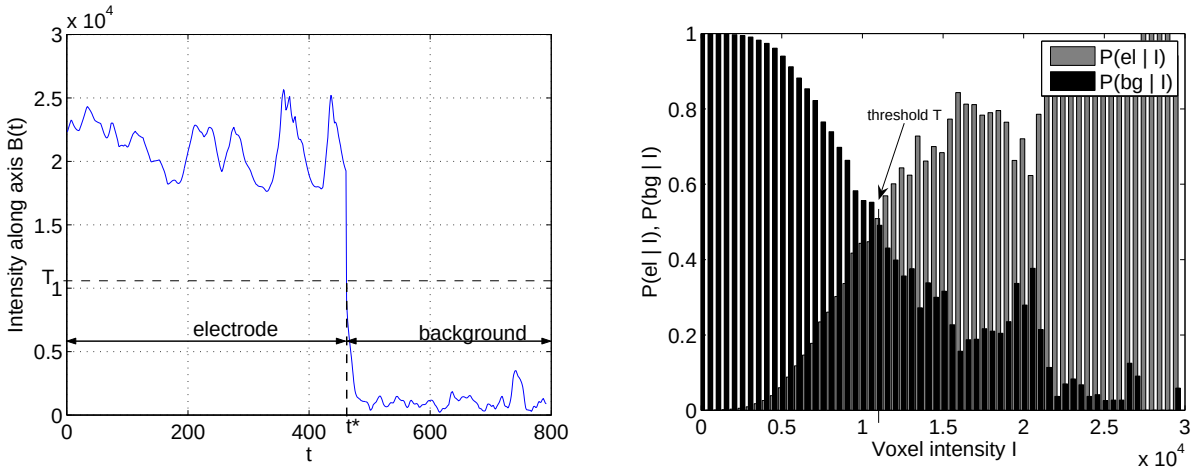

Figure 8: (a) Intensity profile along estimated axis $a(t)$ is used to identify the part of axis that passes through the electrode. (b) Histograms of electrode and background voxels intensities are calculated a priori to approximate the conditional probabilities $P(el \,|\, I)$, $P(bg \,|\, I)$.

voxels.

3 Experiments

Two types of 3D ultrasound images were used to test the algorithm robustness: (i) numerical phantoms simulated using the FILED II software package (ii) real ultrasound images acquired with a 3D ultrasound scanner.

3.1 Accuracy assessment

Two measures were used to quantify the accuracy of the proposed method. The first measure ε_{tip} evaluates the tip localization accuracy

$$\varepsilon_{tip} = \left\| T - \hat{T} \right\|, \tag{15}$$

where E is the intercept point[2], T the true electrode tip, $\hat{T}$ an estimated tip, $a(t)$ an estimated axis and $\|\cdot\|$ is the Euclidean distance.

[2]nazev prevzat z clanku [10]

Axis localization accuracy ε_{axis} is given by

$$\varepsilon_{axis} = \max\left\{\|E - Q_1\|, \|T - Q_2\|\right\}, \tag{16}$$

where Q_1, Q_2 are the orthogonal projections of E, T on $a(t)$ with respect to the true axis.

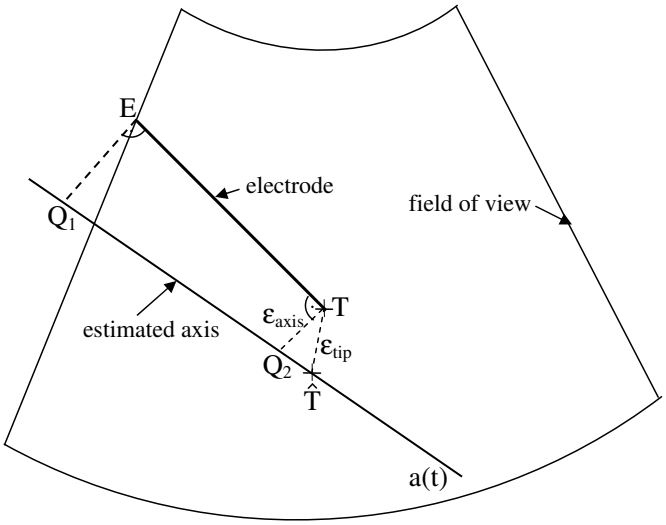

Figure 9: Illustration of axis and endpoint accuracy evaluation. Ground-truth electrode position is determined by the intercept point E and electrode tip T. We compare it with an axis $a(t)$ and the tip $\hat{T}$ estimated by the proposed method.

3.2 Numerical phantom

Simulated data were generated using the ultrasound simulator FIELD II [18]. The simulator parameters were set to imitate the ultrasound scanner Voluson 530D (Kretztechnik, Zipf, Austria). We used a multi-element transducer to produce a sequence of 2D sector scan planes of tilt angle 40° composed of 71 scan lines. In total 53 scan planes were angularly distributed over tilt angle of 40° to scan a 3D region. Table 1 summarizes the parameters set in FIELD II. The dimensions of the point spread function of the ultrasound system were set to 0.2 mm in axial and 1 mm in both lateral and azimuthal directions.

We simulated a series of numerical phantoms representing a cuboid region of tissue containing a highly reflecting inclusion corresponding to a metallic electrode. The dimensions

transducer type	linear array
number of elements	128
element width [mm]	0.4
element height [mm]	5
kerf [mm]	0.025
initial focus [mm]	[0 0 55]
central frequency [MHz]	7.5
sampling frequency [MHz]	27

Table 1: Parameters of FIELD II used for simulation of numerical phantoms.

of the tissue region were 50x50x30 mm and its axial distance from the probe was set to 35 mm. To approximate the speckle pattern of biological tissue, the spatial density of tissue diffusers was set to 3 per mm^3. Their reflection coefficients had normal distribution with zero mean and variance equal to 1 [19]. The electrode was represented by a cylindrical region of 0.3 mm in diameter containing diffusers with spatial density 125 per mm^3. Their reflection coefficients were constant and equal to 5. Figure 10 depicts an example of a 3D numerical phantom simulated in FIELD II. The exact knowledge of electrode axis and tip location is used to evaluate the algorithm accuracy.

3.2.1 Influence of angular step size

The accuracy of the PIP method is good if the angular step parameter Δ^{final} is small. However, this leads to an increase in computational time. To find the optimal value of Δ^{final} we simulated a numerical phantom with an electrode of the length 20 mm. The electrode axis position was estimated by the algorithm while varying Δ^{final} from 0.125° to 32°. Other parameters were constant: $\Delta^{init} = 32°$, and $\Delta_u = \Delta_v = 0.2$ mm.

Figure 12 illustrates axis localization accuracy ε_{axis} as a function of Δ^{final}. We conclude that decreasing this parameter under 1° leads to an increase in computational time (Figure 11) without further improvement in axis accuracy. We set Δ^{final} to 1°.

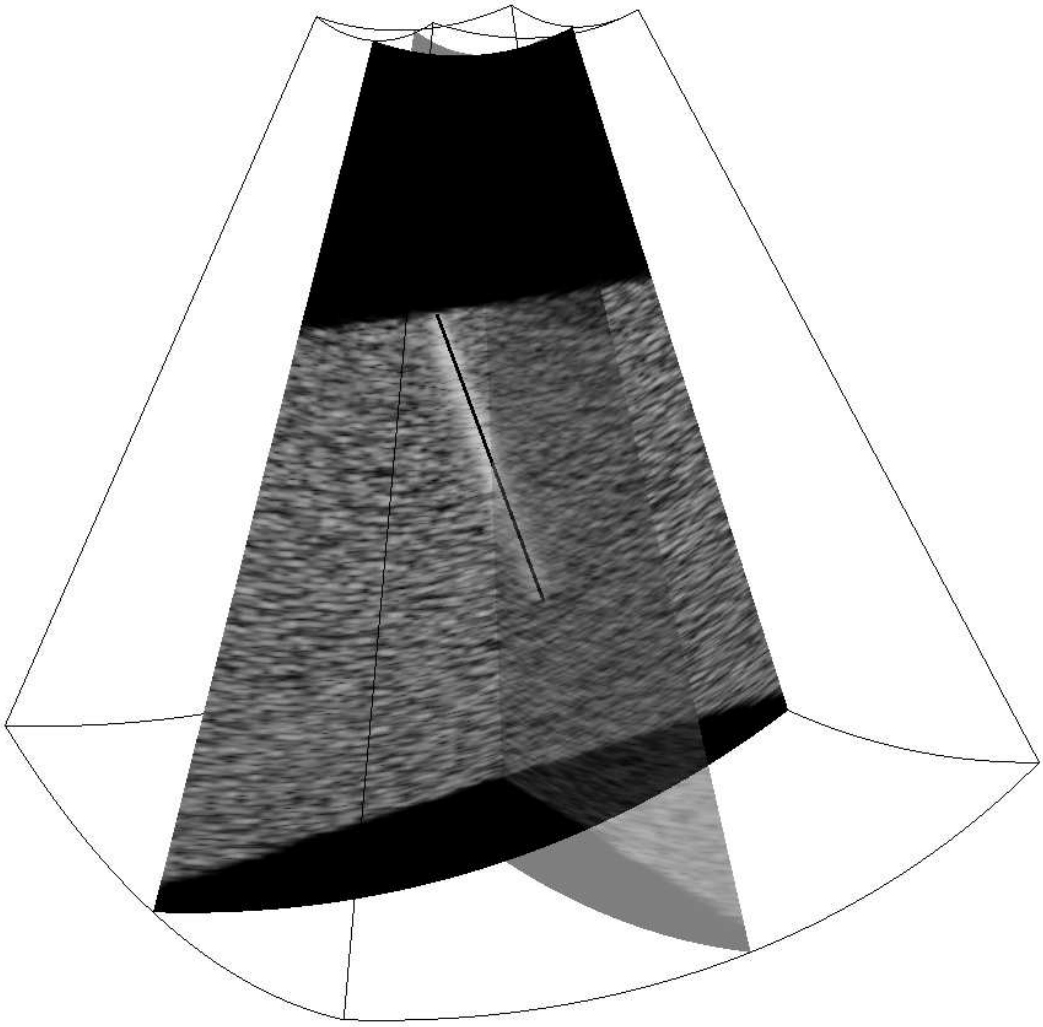

Figure 10: Example of a 3D numerical image simulated in FIELD II. It represents a portion of biological tissue containing a highly scattering inclusion such as electrode. Two planar sections are shown in grayscale; one of them is passing through the electrode axis. Black line-segment depicts electrode position estimated by the proposed method.

3.2.2 Influence of displacement steps Δ_u, Δ_v

The displacement parameters Δ_u, Δ_v control the distance between adjacent lines of integration. While decreasing these parameters improves the accuracy, it increases the computational time (Figure 13). The same numerical phantom as in Section 3.2.1 was used to experimentally determine optimum values of Δ_u, Δ_v. The localization algorithm was executed several times

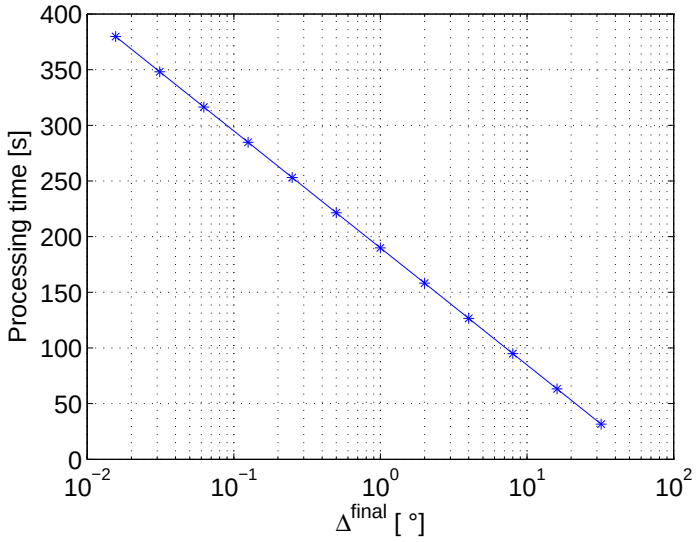

Figure 11: Time required to maximize the PIP transformation for various values of Δ^{final} with other parameters set to constants.

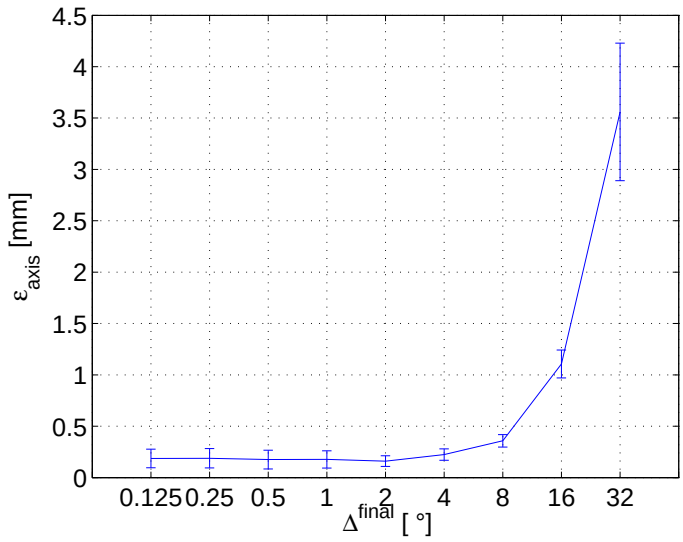

Figure 12: The effect of varying the final angular step Δ^{final} on axis localization accuracy ε_{axis}.

with fixed parameters $\Delta^{init} = 32°$, $\Delta^{final} = 1°$ and varying the displacement steps Δ_u, Δ_v from 0.0625 to 2 mm.

Figure 14 depicts the calculated axis accuracy ε_{axis} as a function of the displacement steps

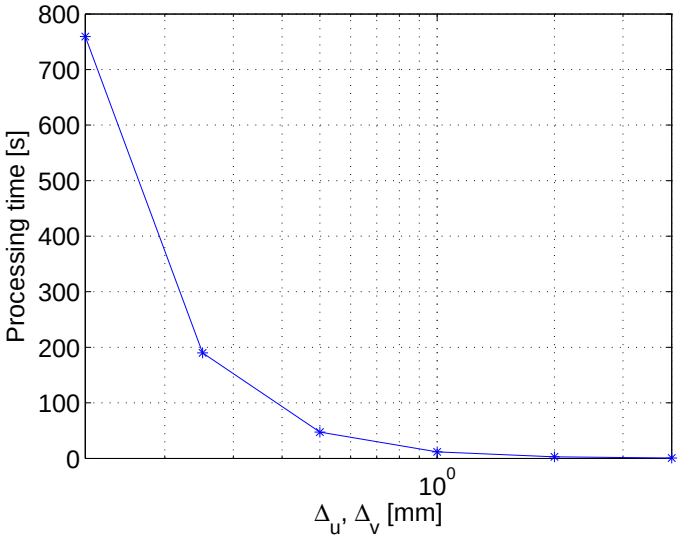

Figure 13: Time required to maximize the PIP transformation for various values of Δ_u, Δ_v with other parameters set to constants.

Δ_u, Δ_v. It shows that when Δ_u, Δ_v exceeds 0.25 mm, the mean and standard deviation of error in axis localization increases rapidly. We propose to set Δ_u, Δ_v to 0.2 mm.

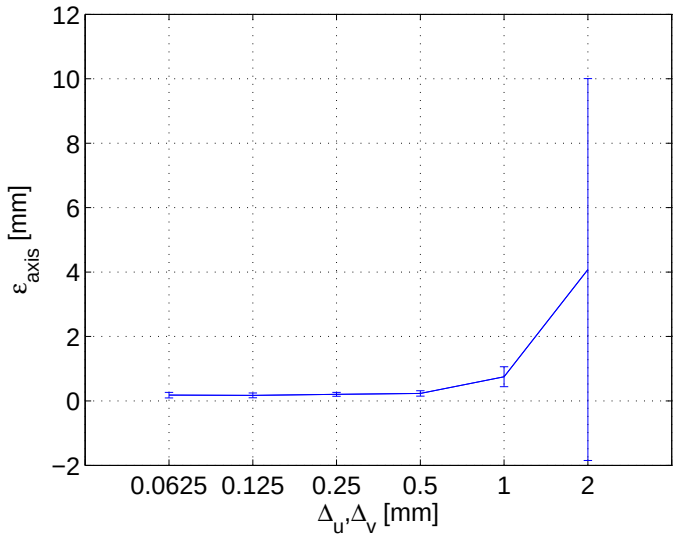

Figure 14: Axis localization accuracy ε_{axis} as a function of discretization steps Δ_u, Δ_v.

3.2.3 Effect of background noise

In real applications, the intensity of electrode and background voxels varies randomly. To investigate the influence of background noise, we simulated fourteen numerical phantoms with the electrode at the same position while increasing the background noise. Given the mean μ_{bg}^2 and the variance σ_{bg}^2 of background voxels and the mean μ_{el}^2 and the variance σ_{el}^2 of electrode voxels, we determine a SNR parameter as the logarithm of the power of electrode to background voxel intensities,

$$\mathrm{SNR} = 10 \log \frac{\mu_{el}^2 + \sigma_{el}^2}{\mu_{bg}^2 + \sigma_{bg}^2} \ \mathrm{[dB]} \tag{17}$$

The value of SNR is used quantify the ratio of electrode intensity to background noise. The electrode axis was localized in each phantom with fixed parameters: $\Delta^{init} = 32°$, $\Delta^{final} = 1°$ and $\Delta_u = \Delta_v = 0.2$ mm.

Experimental dependences of ε_{axis}, ε_{tip} on SNR are depicted in Figure 15. When background noise was increased, we observed decrease in both axis and tip localization accuracy. The axis localization error grows rapidly for SNR inferior to 9 dB.

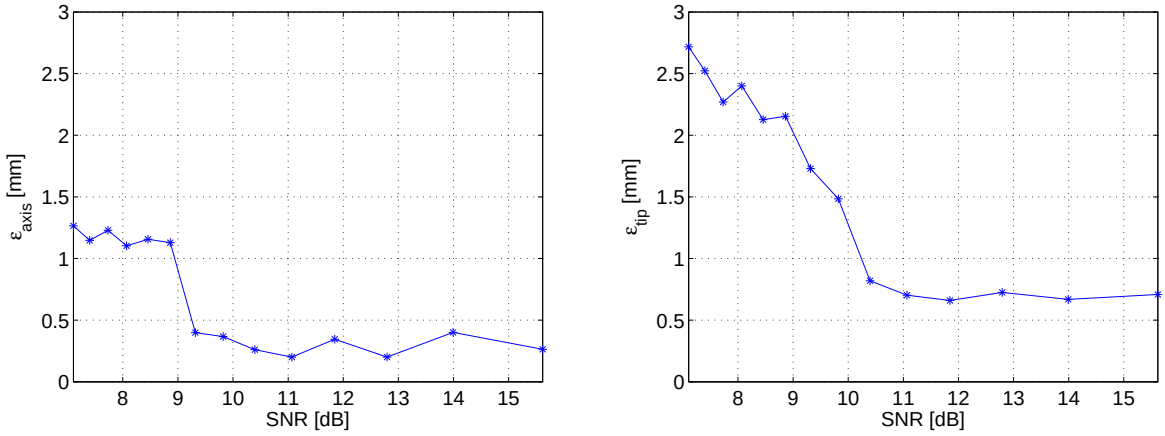

Figure 15: The dependence of axis and tip localization accuracy on image SNR.

3.2.4 Varying electrode orientation and position

The angle γ between the electrode axis and the probe axis was varied from 0° to 160°. The electrode axis and tip were localized in each phantom using the localization algorithm with

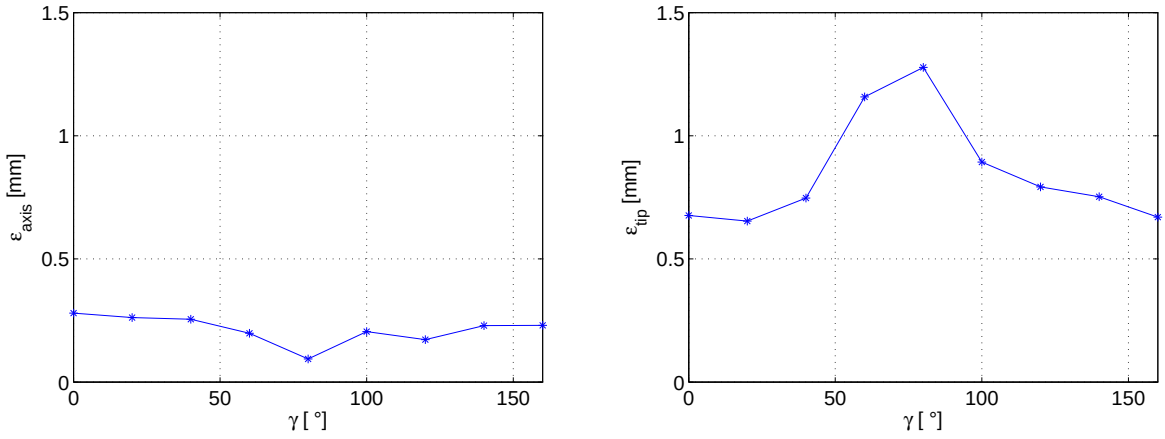

Figure 16: Axis and tip localization accuracy as a function of electrode orientation with respect to probe axis.

the same settings as in Section 3.2.3.

Localization accuracy ε_{axis}, ε_{tip} are shown in Figure 16 as a function of electrode orientation. Note that axis accuracy ε_{axis} is high for $\gamma = 90°$, whereas the tip accuracy ε_{tip} is low. This is a consequence of an anisotropic spatial resolution of ultrasound system.

3.3 Cryogel phantom

The algorithm was tested on real 3D ultrasound data as well. To simulate biological tissue with a highly reflecting inclusion, a polyvinyl alcohol (PVA) cryogel phantom [20] with the dimensions 50x50x50 mm was employed. Inside the phantom there was a thin tungsten electrode of 150 μm in diameter and length 20 mm (Figure 17).

The phantom was scanned with a 3D ultrasound scanner Voluson 530D equipped with a mechanically tilted transducer operating at central frequency 7.5 MHz. Tilt angle was set to 40° at interval 0.75°. The angle of acquired B-mode sector images was 40° with the angular step 0.5°. The phantom orientation and distance from the probe was slightly varied between scanning to obtain eight 3D images of 1000x1000x1500 voxels (Figure 18).

To evaluate the accuracy ε_{axis} and ε_{tip}, the intercept and electrode tip coordinates were manually determined in each dataset and considered as the ground-truth. Table 2 summarizes

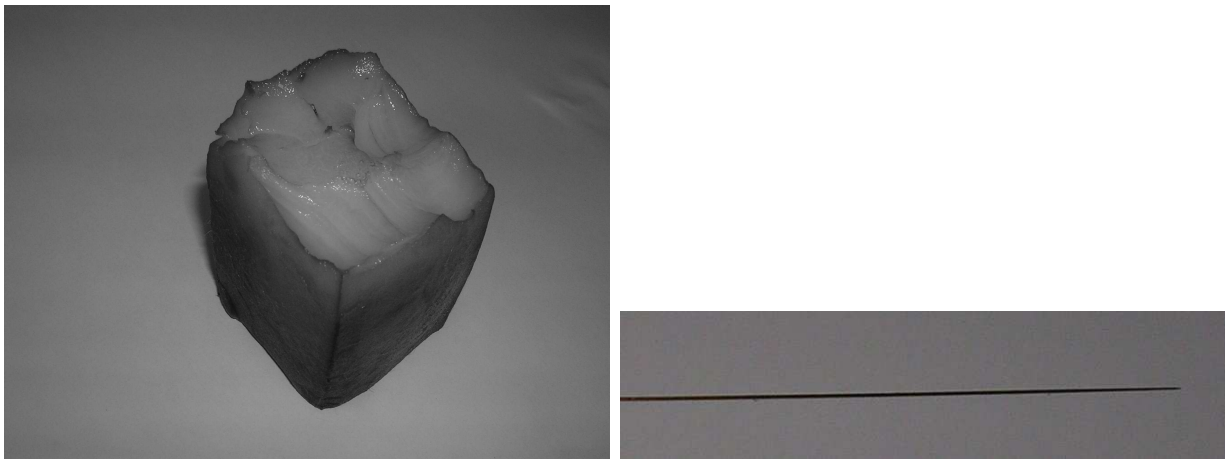

Figure 17: (a) Cuboid of polyvinyl alcohol cryogel phantom mimicking acoustic properties of biological tissue. (b) Tungsten electrode of 150 μm in diameter was introduced into the phantom prior to scanning.

the localization accuracy for each ultrasound image.

#image	1	2	3	4	5	6	7	8	mean/median
ε_{axis} [mm]	0.231	0.096	0.203	0.248	0.103	0.237	0.081	0.212	0.176 / 0.208
ε_{tip} [mm]	0.936	0.858	0.827	0.887	0.858	0.791	0.756	0.871	0.848 / 0.858

Table 2: Achieved localization accuracy on real ultrasound images.

4 Conclusion

The use of 3D ultrasound imaging modality in image-guided interventions is increasing. In many of these applications, it is important to determine the position of a needle and its tip. We propose a new technique for electrode localization in a 3D ultrasound image. It permits to automatically determine the electrode axis and the electrode tip. The axis is found by maximizing the Parallel Integral Projection transform. A hierarchical mesh-grid search is used to accelerate this task. The tip position is determined by optimal thresholding of voxel intensities along the estimated axis.

The experiments performed on numerical phantoms shows that the localization is robust

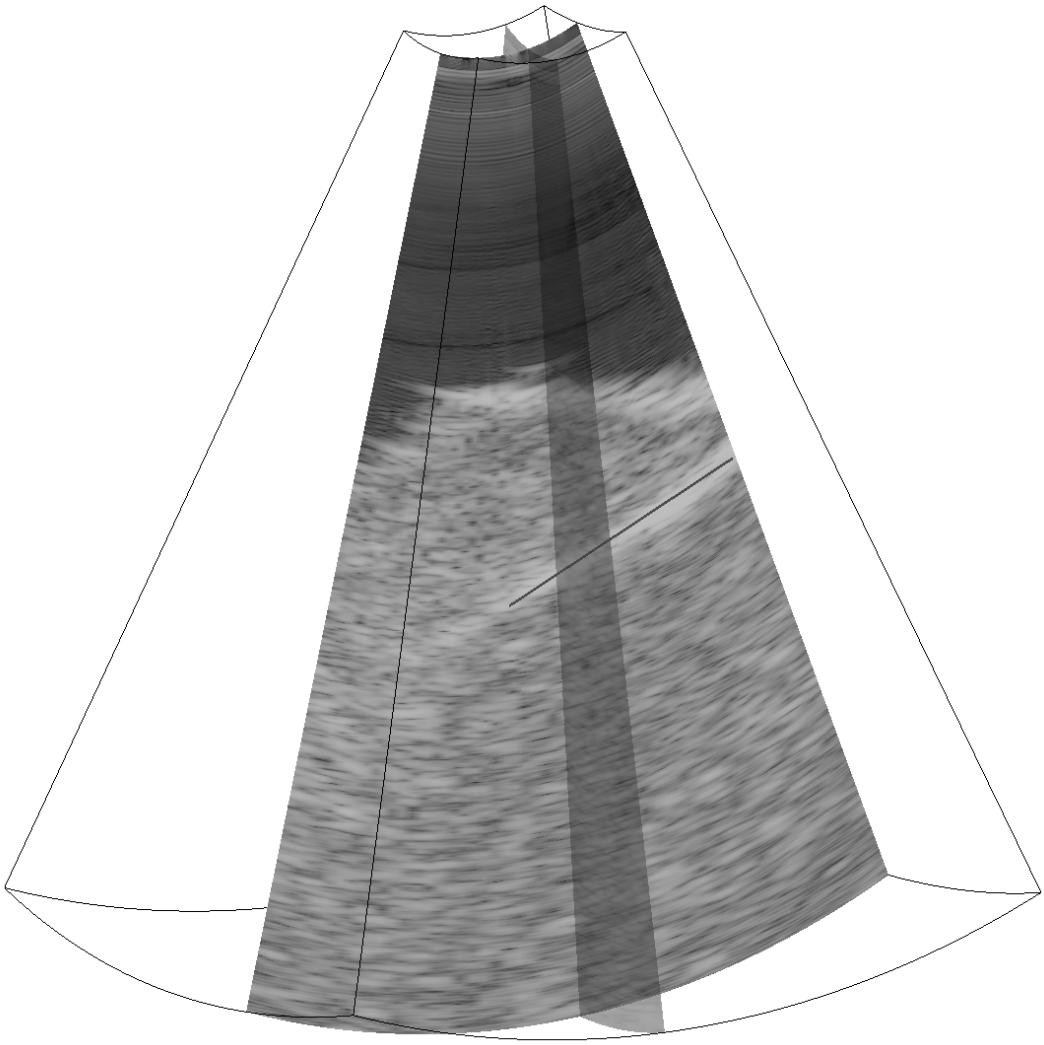

Figure 18: Example of 3D ultrasound image of PVA cryogel phantom submerged in water. Inside the phantom there was a tungsten electrode. Two planar sections (one of them passing through the electrode axis) are shown in grayscale. Black line-segment represents estimated electrode position.

with respect to the background noise and the accuracy does not depend significantly on the electrode orientation. Achieved localization accuracy is of the order of hundreds of micrometers and is comparable to the axial resolution of the ultrasound system. The consistence of the results obtained on numerical phantoms and real 3D ultrasound data of a PVA phantom suggests that this approach is both robust and accurate under realistic conditions. The pro-

cessing time of the current algorithm implementation in MATLAB is tens of minutes. But rewriting the method in a compiled language such as C/Java should accelerate the localization process.

References

[1] A. Abati and A. Simsir. Breast fine needle aspiration biopsy: prevailing recommendations and contemporary practices. *Clinics in laboratory medicine*, 25(4):631–654, December 2005.

[2] K. Kern. Sentinel lymph node mapping in breast cancer using subareolar injection of blue dye. *Journal of the American College of Surgeons*, 189(6):539–545, December 1999.

[3] R. L. Alterman, D. Sterio, A. Beric, and P. J. Kelly. Microelectrode recording during posteroventral pallidotomy: Impact on target selection and complications. *Neurosurgery*, 44(2):315–321, February 1999.

[4] V. Horsley, , and R.H. Clarke. The structure and functions of the cerebellum examined by a new method. *Brain*, 31:45–124, 1908.

[5] L. S. Scott, P. Douglas, G. H. Baltuch, and J. L. Jaggi. Error analysis of MRI and Leksell stereotactic frame target localization in deep brain stimulation surgery. *Stereotactic and functional neurosurgery*, 83(1):1–5, 2005.

[6] A. Schweikard, G. Glosser, M. Bodduluri, M. J. Murphy, and J. R. Adler. Robotic motion compensation for respiratory movement during radiosurgery. *Computer Aided Surgery*, 5(4):263–277, 2000.

[7] S. Krueger, F. Vogt, W. Hohenberger, D. Paulus, H. Niemann, and C. H. Schick. Evaluation of computer-assisted image enhancement in minimal invasive endoscopic surgery. *Methods of Information in Medicine*, 43:362–366, 2004.

[8] P. W. Glimcher, V. M. Ciaramitaro, M. L. Platt, H. M. Bayer, M. A. Brown, and A. Handel. Application of neurosonography to experimental physiology. *Journal of Neroscience Methods*, 180:131–144, 2001.

[9] J. W. Cannon, J. A. Stoll, and I. S. Salgo. Real time 3-dimensional ultrasound for guiding surgical tasks. *Computer aided surgery*, 8:82–90, 2003.

[10] K. J. Draper, C. C Blake, D. B. Gowman, L. nad Downey, and A. Fenster. An algorithm for automatic needle localization in ultrasound-guided breast biopsies. *Medical Physics*, 27:1971–1979, 2000.

[11] P. M. Novotny, J. W. Cannon, and R. H. Howe. Tool localization in 3D ultrasound images. In *Proceedings of Medical Image Computing and Computer-Assisted Intervention*, volume 2879, pages 969–970. Springer-Verlang, Berlin, 2003.

[12] L. Tao, U. Castellani, A. Fusiello, and V. Murino. 3D acoustic image segmentation by a RANSAC-based approach. In *Proceedings of Oceans 2003 Marine Technology and Ocean Science Conference, San Diego, USA*, pages 1098–1101, September 2003.

[13] M. A. Fischler and R. C. Bolles. Random sample consensus: A paradigm for model fitting with applications to image analysis and automated cartography. *CACM*, 24(6):381–395, June 1981.

[14] M. Ding, H. N. Cardinal, W. Guan, and A. Fenster. Automatic needle segmentation in 3D ultrasound images. In *Proceedings of SPIE*, volume 4681, pages 65–76. International Society for Optical Engineering, May 2002.

[15] F. Natterer. *The Mathematics of Computerized Tomography*. Society for Industrial and Applied Mathematics, classics in applied mathematics edition, 2001.

[16] E. Heitz, P. Perez, and P. Bouthemy. Multiscale minimization of global energy functions in some visual recovery problems. *Computer Vision, Graphics, and Image Processing*, 59(1):125–134, 1994.

[17] R. Bulirsch and J. Stoer. *Introduction to Numerical Analysis.* Springer-Verlag, New York, 1991.

[18] J. A. Jensen. Field: A program for simulating ultrasound systems. In *Medical and Biological Engineering and Computing*, volume 34, pages 351–353, 1996.

[19] J. A. Jensen and Munk P. Computer phantoms for simulating ultrasound B-mode and CFM images. *Acoustical Imaging*, 23(75–80), 1997.

[20] K. C. Chu, , and B. K. Rutt. Polyvinyl alcohol cryogel: An ideal phantom material for mr studies of arterial flow and elasticity. *Magnetic Resonance in Medecine*, 37(2):314–319, 1997.